

Two rate periodic protocol with dynamics driven through many cycles

Satyaki Kar

Theoretical Physics Department, Indian Association for the Cultivation of Science, Jadavpur, Kolkata-700032, India.

(Dated: September 21, 2018)

We study the long time dynamics in closed quantum systems periodically driven via time dependent parameters with two frequencies ω_1 and $\omega_2 = r\omega_1$. Tuning of the ratio r there can unleash plenty of dynamical phenomena to occur. Our study includes integrable models like Ising and XY models in $d = 1$ and Kitaev model in $d = 1$ and 2 and can also be extended to Dirac fermions in graphene. We witness the wave-function overlap or dynamic freezing to occur within some small/ intermediate frequency regimes in the (ω_1, r) plane (with $r \neq 0$) when the ground state is evolved through single cycle of driving. However, evolved states soon become steady with long driving and the freezing scenario gets rarer. We extend the formalism of adiabatic-impulse approximation for many cycle driving within our two-rate protocol and show the near-exact comparisons at small frequencies. An extension of the rotating wave approximation is also developed to gather an analytical framework of the dynamics at high frequencies. Finally we compute the entanglement entropy in the stroboscopically evolved states within the gapped phases of the system and observe how it gets tuned with the ratio r in our protocol. The minimally entangled states are found to fall within the regime of dynamical freezing. In general, the results indicate that the entanglement entropy in our driven short-ranged integrable systems follow genuine non-area law of scaling and show a convergence (with a r dependent pace) towards volume scaling behavior as the driving is continued for long time.

PACS numbers: 73.43.Nq, 05.70.Jk, 64.60.Ht, 75.10.Jm

I. INTRODUCTION

Dynamics of closed quantum many body system, driven out of equilibrium has become an engaging research field in recent times¹⁻³. Many interesting physics such as universal scaling of excitation density during slow quenches⁴⁻⁹ through a quantum critical point (QCP), quantum coherence^{10,11} or dynamical phase transitions (DPT) leading to cusp-like features in Lochsmidt echo pattern¹²⁻¹⁶ has already surfaced in the literature. At the same time, experimental realization of such closed quantum system has also become possible using trapped ultracold atoms in optical lattices¹⁷ and thus enabling hands-on check for the related theories put forward. Non-equilibrium dynamics of various integrable and non-integrable systems of, for example transverse field Ising (TFIM), XY (TFXYM) or Bose-Hubbard type, can be well emulated these days.

A linear quench to drive a system out of equilibrium and the corresponding Kibble Zurek (KZ) mechanism^{2,4} for defect production as it passes through a QCP has been studied for quite some time. Study of periodic driving, in comparison, is rather new. A periodic protocol allows multiple passage of the system through quantum critical points exhibiting novel features like stueckelberg interference, dynamical freezing, dynamical phase transitions (DPT) or steady periodic states¹⁸⁻²¹. In most of these studies, single-frequency periodic protocols are used to drive the system and examine the resulting dynamics. Recently Kar *et al.*²² considered a two rate periodic protocol where both the energy bias and detuning in the underlying two level system (TLS) are treated periodically with time. The low frequency regime that they study there, reveals signatures of dynamical freezing as driving for one complete cycle is performed. Such low frequency freezing was hitherto unobserved from the single-rate periodic driving examined so far. For a TFXYM, such freezing occurs mostly around the point where both the periodic functions have same frequen-

cies, though other class of systems like tilted Bose-Hubbard, Kitaev models or Dirac fermions can show such phenomena in their respective other discrete frequency regimes²². In this present paper, we probe such dynamics stroboscopically as the two-rated driving is continued for long time. The alteration in the defect profile is witnessed as we scan through small to large values in the frequency space. We find that further regimes of freezing to sprout in the intermediate, not so-large frequencies and discuss their evolution as the driving is continued stroboscopically for longer times. We analyze the correlation functions, magnetization and also the behavior of entanglement entropy under such long driving.

Unlike a linear or any other aperiodic drive, a periodic drive, as mentioned before, unleashes rich set of dynamical phenomena^{18-21,23-25}, even more so, if driven by two rate protocols²². Repeated passage through the critical points give the system, initially in its ground state, ample chances to move to the excited states and experience the quantum interference of the probability waves at the crossing/ avoided crossing regions. A drive through a number of cycles allows more exposure to such QCP's resulting in alteration of the exotic dynamical responses witnessed within a short time. Particularly, the high degree of dynamics induced freezing^{21,24,26,27} which implies almost complete overlap of the initial and final wavefunction, is obtained with a two-rate protocol just by driving for a single-cycle²². Though the phenomenon, when viewed stroboscopically, stays alive for a while, a long driving tone down the temporal fluctuations of the observables making the freezing scenario rarer. This paper reports results of a 1D TFXYM where such freezing takes place for drive frequency ω_1 as small as unity at $r \sim 1$ ($r = \omega_2/\omega_1$, ω_2 being the other frequency in the two-rate protocol). A scan through larger frequencies sees spreading of such freezing zone around $r = 1$ as well as new freezing patches to sprout at $\omega_1 \sim 10$ for $r \sim 0.5$ and 2.0, within the ranges shown. With continued spreading for larger ω_1 , freezing gradually takes over the frequency

space, for r not very small. A small ω_2 makes the actual period of the drive very large causing measurements after integral time periods corresponding to ω_1 not truly stroboscopic. However, a long drive brings in the steady states soon where the transient behaviors, due to temporal fluctuations die out resulting in less amount of freezing in the system.

This paper also discusses analytic tools that can well describe the dynamics under the drive with a two rate protocol. The adiabatic-impulse approximation, used initially in Ref.22 for similar protocol, is extended for stroboscopic long driving and for larger ranges of frequencies. It turns out to capture the final evolved states at small frequencies quite well even after passage through many cycles. At high frequency regime, a rotating wave approximation is a well known formalism for obtaining a faithful description of the dynamics. Here we extend the idea to incorporate it to the two rate periodic protocols of ours. The dynamics followed by such two rate protocols thus can be well accounted for via analytic frameworks both for small and large frequencies.

Walking down the line, estimating quantum entanglement and its time evolution in the evolved states carries huge importance from the quantum information perspective. And the bipartite entanglement entropy is a good measure of such entanglement in the quantum system. In a many body system of size L^d (d being the dimension), the Von-Neuman entropy S of a sub-system of size l^d can be computed from the reduced density matrix ρ as $S = -\text{Tr}[\rho \ln \rho]$. For the two-rate protocol, r can be treated as a tuning parameter for controlling the system entanglement. We find that the region of dynamic freezing identifies the minimally entangled states. The ground state in a gapped system, corresponding to a short-ranged Hamiltonian, obeys an area scaling law for the entropy, *i.e.*, $S \sim l^{d-1}$ (For $d = 1$, this is called the Hastings' theorem²⁸). We see that the entanglement entropy $S_n(l)$, after drive through n cycles, shows such area scaling only when driven for a few number of cycles (*i.e.*, n small), but a non-area scaling $S \sim l^\alpha$ appears with $\alpha > d - 1$ for large n values. This amounts to a cross-over from a short-ranged to long-ranged behavior as the long drive exposes the system, originally defined with a nearest neighbor short range model, to excitations that are long ranged (described by ground-states of some long-ranged Hamiltonians²⁹). A driving for infinitely long time finally relaxes the system towards a generalized Gibbs ensemble (GGE)¹ with entropy scaling exponent $\alpha \rightarrow d$ (*i.e.*, approaching volume scaling law). This convergence of α towards d , as l is varied, is found to be non-monotonic for small frequencies. We see that using r as a tuning parameter, we can expedite or retard the pace of such convergence.

The plan of the paper is as follows. In section II, we first describe our two-rate periodic protocol and then analyze the time evolution of the system wave-function in a integrable fermionic Hamiltonian (Eq.1) following the Schrodinger equation. Here within subsection A, we report and discuss the results on defect densities and magnetization and then formulate the analytic approaches of adiabatic-impulse approximation and Rotating wave approximation for our two rate protocol showing their validity in the respective slow and large frequency regimes. Then within subsection B,

we discuss the entanglement generation during periodic driving and discuss various results on entanglement entropy. Finally in section III, we summarize our results, discuss their experimental implications, and conclude.

II. FORMULATION AND RESULTS

In this work, our aim is to study the effect of two-rate periodic drive protocols on a class of integrable closed quantum systems. We choose the drive protocol to involve periodic variation of two parameters of the system Hamiltonian with frequencies ω_1 and ω_2 . Our protocol represents a class of models that can be expressed by a general form of free fermionic Hamiltonian $H = \sum_{\vec{k}} \psi_{\vec{k}}^\dagger H_{\vec{k}} \psi_{\vec{k}}$, where $\psi_{\vec{k}} = (c_{\vec{k}}, c_{-\vec{k}}^\dagger)^T$ is the two component fermion field, $c_{\vec{k}}$ denotes fermionic annihilation operator, and $H_{\vec{k}}$ is a 2×2 matrix Hamiltonian density:

$$H_{\vec{k}} = [\lambda_1(\omega_1 t) - b_{\vec{k}}] \tau_3 + \lambda_2(r\omega_1 t) \Delta_{\vec{k}} \tau_1. \quad (1)$$

Here $\lambda_1(\omega_1 t)$ and $\lambda_2(r\omega_1 t)$ are two time-dependent parameters with periodic variations given by frequencies ω_1 and $\omega_2 = r\omega_1$ respectively and τ_3 and τ_1 are Pauli matrices in particle-hole space. Such free fermionic Hamiltonians represents Ising and XY models in $d = 1$ ³² and Kitaev model in $d = 2$ ³³⁻³⁵. Additionally, it can also describe singlet/ triplet superconductors and Dirac-like quasiparticles in graphene³⁶ and on the surface of a topological insulators³⁸. In what follows we shall carry out numerical analysis of this model in the context of XY model in $d = 1$; we note, however, that our results shall be valid for any other representations of $H_{\vec{k}}$.

The XY model in a transverse field constitute a model for of half-integer spins on a one-dimensional (1D) chain having a Hamiltonian

$$H_{XY} = \sum_{\langle ij \rangle, \alpha=x,y} J_\alpha S_i^\alpha S_j^\alpha - h \sum_i S_i^z. \quad (2)$$

Here $J_{x,y}$ are nearest neighbor coupling between x and the y components of the spins, $\langle ij \rangle$ indicates the nearest neighbor sites i and j and h is the transverse field. A Jordan-Wigner transformation³ can map this Eq. 2 to Eq. 1 in $d = 1$ with the identification

$$\begin{aligned} b_k &= (J_x + J_y) \cos(k), & \lambda_1 &= -h \\ \Delta_k &= -i \sin(k), & \lambda_2 &= (J_x - J_y) \end{aligned} \quad (3)$$

So in the two-rate protocol considered, all of the parameters h , J_x and J_y need to be time-periodic.

In a similar manner, the Kitaev model in $d = 2$ can also be mapped into Eq.1. The Hamiltonian of the Kitaev model can be written in terms of half-integer spins residing on the sites

of a honeycomb lattice as

$$H_{k2D} = \sum_{j+l=\text{even}} (J_1 S_{j+1,l}^x S_{j,l}^x + J_2 S_{j-1,l}^y S_{j,l}^y + J_3 S_{j,l+1}^z S_{j,l}^z) \quad (4)$$

where (j, l) denotes coordinates of a site on the honeycomb lattice, and $J_{x,y,z}$ are the coupling strength between neighboring x, y, z components of the spins. It turns out that H_{k2D} can also be mapped to Eq.1 with the identification

$$\begin{aligned} b_{\vec{k}} &= -J_1 \cos(k_1) - J_2 \cos(k_2), & \lambda_1 &= J_3 \\ \lambda_2 \Delta_{\vec{k}} &= J_1 \sin(k_1) - J_2 \sin(k_2), \end{aligned} \quad (5)$$

where $k_{1(2)} = \vec{k} \cdot \vec{M}_{1(2)}$, $\vec{M}_{1(2)} = \sqrt{3}\hat{i}/2 + (-)\hat{j}/2$ are the spanning vectors of the reciprocal lattice and \hat{i} and \hat{j} are the unit vectors in the x and the y directions.

We can make $J_1 = 0$ in Eq. 4 to obtain a Kitaev model in one dimension.

Starting from the many-body ground state, the stroboscopic dynamics displays interesting features in the defect density, magnetization or entanglement profiles. We give a detailed description of the same in the following.

A. Defect production

1. Numerical integration

In this section we will describe the time evolution of the system's wave-function following the Schrodinger equation. In the Jordan-Wigner transformed Hamiltonian, there are $L^d/2$ number (L^d denotes the system size in d dimensions) of independent \vec{k} -modes (involving $(\vec{k}, -\vec{k})$ pair) due to integrability of the system. The two-dimensional subspace spanned by the unoccupied $|0_{+\vec{k}}0_{-\vec{k}}\rangle$ and doubly occupied $|\vec{k}, -\vec{k}\rangle$ fermionic states, at each \vec{k} level, thus constitutes a TLS in this problem^{3,21}. In the time-independent adiabatic basis²³, the instantaneous ground states and excited states for the \vec{k} -mode are given by $|\phi_{-\vec{k}}\rangle = (\beta_{+\vec{k}}(t), \beta_{-\vec{k}}(t))^T$ and $|\phi_{+\vec{k}}\rangle = (\beta_{-\vec{k}}(t), -\beta_{+\vec{k}}(t))^T$ respectively, with

$$\begin{aligned} \beta_{\pm, \vec{k}}(t) &= \sqrt{\frac{E_{\pm, \vec{k}} \pm (\lambda_1(\omega_1 t) - b_{\vec{k}})}{2E_{\pm, \vec{k}}}}, \\ E_{\pm, \vec{k}}(t) &= \pm \sqrt{(\lambda_1(\omega_1 t) - b_{\vec{k}})^2 + \lambda_2^2(r\omega_1 t) \Delta_{\vec{k}}^2}. \end{aligned} \quad (6)$$

A general wave-function at a given momentum \vec{k} is denoted by $|\psi_{\vec{k}}\rangle = (a_{1, \vec{k}}(t), a_{2, \vec{k}}(t))^T$ on the same basis. Now, $b_{\pm, \vec{k}}$ being the probability amplitudes of the state in the eigen-basis $|\phi_{\pm, \vec{k}}\rangle$ (or, the time dependent adiabatic basis), we can write

$$\begin{aligned} a_{1, \vec{k}}(t) &= b_{+, \vec{k}}(t) \beta_{-, \vec{k}}(t) + b_{-, \vec{k}}(t) \beta_{+, \vec{k}}(t) \\ a_{2, \vec{k}}(t) &= b_{-, \vec{k}}(t) \beta_{-, \vec{k}}(t) - b_{+, \vec{k}}(t) \beta_{+, \vec{k}}(t). \end{aligned} \quad (7)$$

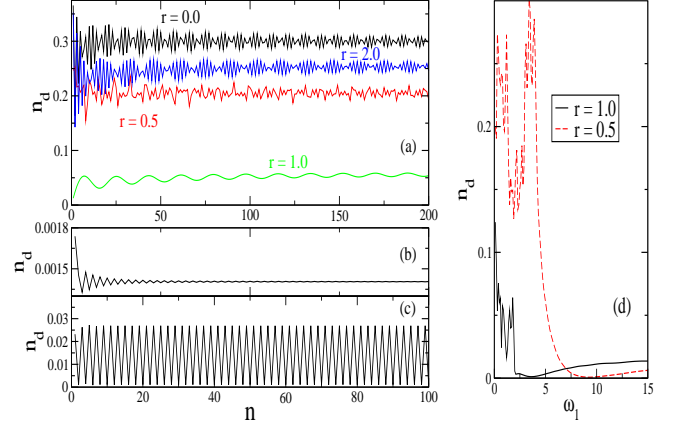


FIG. 1: (Color online) Plot of the defect density n_d of the 1D XY model in a transverse field as a function of number of drive cycle n for (a) drive frequency $\omega_1 = 1$ with $r = 0, 0.5, 1.0$ and 2.0 . (b) drive frequency $\omega_1 = 4$ with $r = 1$. (c) drive frequency $\omega_1 = 10$ with $r = 0.5$. Dynamic freezing observed in (b) and (c) can also be seen from the n_d versus ω_1 plot in (d) for $n = 20$. Here we have chosen $J_x + J_y = 1$, $J_x - J_y = \cos(r\omega_1 t)$, and $h = A \cos(\omega_1 t)$ with $A = 4$.

We start from the instantaneous ground state at $t = 0$ and thus we have $a_{1, \vec{k}}(0) = \beta_{+, \vec{k}}(0)$ and $a_{2, \vec{k}}(0) = \beta_{-, \vec{k}}(0)$. At the final time T , we obtain $b_{+, \vec{k}}(T) = a_{1, \vec{k}}(T) \beta_{-, \vec{k}}(T) - a_{2, \vec{k}}(T) \beta_{+, \vec{k}}(T)$. The excitation or defect density ($n_d(T_f)$) at time T_f is given by the sum of probabilities for being at the excited adiabatic levels, *i.e.*,

$$n_d(T_f) = \sum_{\vec{k}} |b_{+, \vec{k}}(T_f)|^2. \quad (8)$$

Our results are obtained mainly on a 1D TFXM. For that we first choose the parameters $\lambda_{1(2)}$, $b_{\vec{k}}$, and $\Delta_{\vec{k}}$ to be those for a spin- $\frac{1}{2}$ XY chain in a transverse field (Eq. 3) with $\lambda_1 = -h = A \cos(\omega_1 t)$ and $\lambda_2 = \cos(r\omega_1 t)$. Furthermore we consider $J_{x(y)} = (1 + (-)\lambda_2)/2$. While discussing XY model throughout this paper, we consider a fixed amplitude $A = 4$, the value same as that was used in Ref.22 to produce their main results. With driving for long enough, we witness $n_d(T_f)$ to converge to some steady values (see Fig. 1(a)). All our measurements are stroboscopic, in terms of the periodic bias signal having frequency ω_1 (*i.e.*, the time difference between the initial and final states are given by $nT = n \frac{2\pi}{\omega_1}$, n being an integer). Ref.22 shows that dynamic freezing or almost complete overlap between initial and final wave-functions occurs nicely with the two-rate protocol, mostly for $r = 1$, when observed after one cycle of driving with frequency ω_1 . A scan through higher frequency regime reveals that such freezing zones grows with driving frequency, even sprouting new freezing patches around $r \sim 0.5$ and 2.0 (within the regions shown in Fig. 2) for $\omega_1 \sim 10$ and beyond. We should mention here that freezing increases for very small and very large frequencies as $|b_{+, \vec{k}}(T_f)| \rightarrow 0$ for all \vec{k} values in those situations. This can be reasoned nicely using an adiabatic-impulse model

to be discussed in the next sub-section. Long stroboscopic driving smoothens out the temporal fluctuations in transient times and causes freezing phenomena to go rarer.

Fig.1(a) shows defect densities in a transverse field XY chain for different r values as a function of driving cycle number n for a frequency $\omega_1 = 1$. Defect production tends to saturate as n is increased gradually. The fluctuations above the steady value seems to have a period which is multiple of $2\pi/\omega_1$, if r is zero or an integer. We see that the plot for $r = 1$ shows little defect productions compared to that shown for other r values as the transition probability for a single passage through QCP for $r = 1$ can be shown, in this case, to close to unity as compared to its $r = 0$ counterpart (also see Ref.22). The temporal evolution of n_d is also more smooth for $r = 1$.

We witness a low frequency freezing for $3 \leq \omega_1 \leq 5$ for $r = 1$ as well as a high or intermediate frequency freezing for $r = 0.5$ at $\omega_1 \sim 10$. The corresponding plots can be seen in Fig.1(b)-(d). Fig.1(b),(c) show the defect evolution with time for the corresponding cases (see that, Fig.1(c) corresponds to $r = 0.5$ and thus the overall periodicity is observed in units of 2 cycles) while Fig.1(d) demonstrates those freezing regimes for $n = 20$. Fig.2(a) shows the defect density profile in the frequency space for $n = 1$. An ultra-high frequency freezing is a common phenomena for measurements done stroboscopically. But the interesting thing to notice here is the dependence of the low ω_1 cut-off, so to say, on ω_2 values, beyond which freezing continues as ω_1 is increased further. A perfect freezing implies an unaltered state and thus any state variable will retain its values at freezing. The transverse magnetization $m_z(t)$ in the driven state can be defined as

$$m_z(t) = 2L^{-d} \sum_{\vec{k}} |a_{1\vec{k}}(t)|^2 - 1. \quad (9)$$

It thus gives a measure of occupation probabilities of the wave-function in the diabatic basis and its change between initial and final time indicates a state change. In Fig.2(b)-(c), the magnitudes of the change in $m_z(t)$ (let's call it Δm_z) are shown for dynamics after single cycle as well as after 100 cycles corresponding to ω_1 . As freezing implies complete or almost complete overlap of the initial and final wave-functions, the change in $m_z(t)$ should tend to zero under such scenario. Here we demonstrate that from the similarities of the regions $\Delta m_z \sim 0$ in Fig.2(b) with the regimes of $n_d \sim 0$ in Fig.2(a). As with long driving, the system tends towards the steady state, the transient freezing behaviors get rarer as can be seen from Fig.2(c). For example, The freezing points of the (ω_1, r) plane, shown in Fig.1(d) for $n = 20$ existed within the huge freezing zone of Fig.2(a),(b) at $n = 1$, continues to exist at $n = 100$ in Fig.2(c). However the freezing seen around $r \sim 2$ for $\omega_1 \sim 10$ at $n = 1$ falls short at $n = 100$, or even much before at $n = 20$.

The freezing region around $r = 1$ is already known to appear for a driving through a single cycle²² (Fig2(b) of this paper and Fig.5 of Ref.22 can be compared in this regard). And here we show that freezing starts developing for other r values as well when a larger range of ω_1 values are considered.

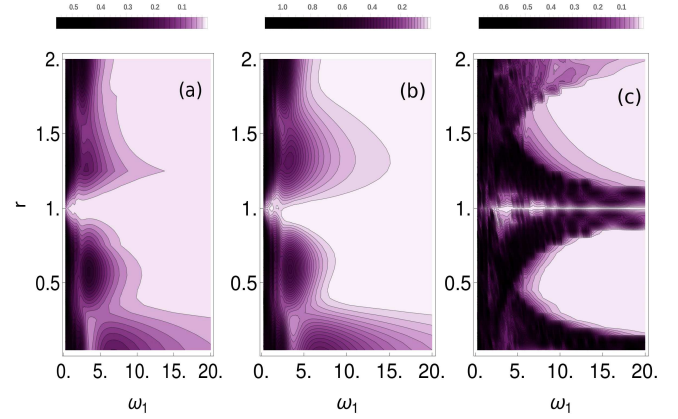


FIG. 2: (Color online) Results from 1D TFXYM. (a) Defect density profile and (b) magnitude of the change in magnetization (Δm_z) within a (ω_1, r) window after driving through $n = 1$ cycles. (c) Δm_z for $n = 100$. All parameters are same as in Fig. 1.

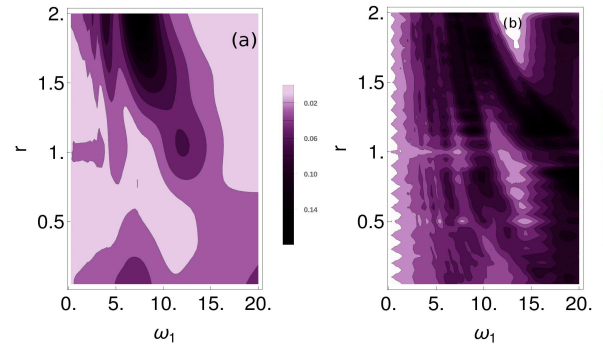


FIG. 3: (Color online) Defect density n_d in a 2D Kitaev model within a (ω_1, r) window after driving through (a) $n = 1$ and (b) $n = 10$ cycles. All parameter values are given in subsection IIA1.

Moreover the freezing condition remains intact as ω_1 is increased further. However, after a long drive corresponding to $n = 100$, the freezing scenario wears off as in a long time evolution the evolved state spreads out more within the Hilbert space leaving less chances for the final state to be close to the initial state in the phase space. Fig.2(c) shows regime about $r = 0.5$ and $r = 1.5$ where Δm_z is small, but it is still larger compared to that of the freezing zones observed at $n = 1$. We also notice that the range of variation in Δm_z reduces as we compare the results for $n = 1$ with $n = 100$, which indicates that after long time, the dynamics relaxes within a low-energy sector of states where magnetization does not vary much.

We also show in Fig.3 defect density profile in the (ω_1, r) space for 2D Kitaev model on a honeycomb lattice with $J_1 = J_2 = [1 + \cos(\omega_2 t)]$ and $J_3 = 4.5[2 + \cos(\omega_1 t)]$, as in Eq.5. It also demonstrate the same feature of reduction of dynamic freezing as system is exposed to long driving. One distinctive feature that we can readily see here is that unlike XY chain results, the 2D Kitaev model defect density profile shows pockets of dynamic freezing in the (ω_1, r) plane. This can happen due to the stuckelberg interference²³ to be discussed in the next sub-section.

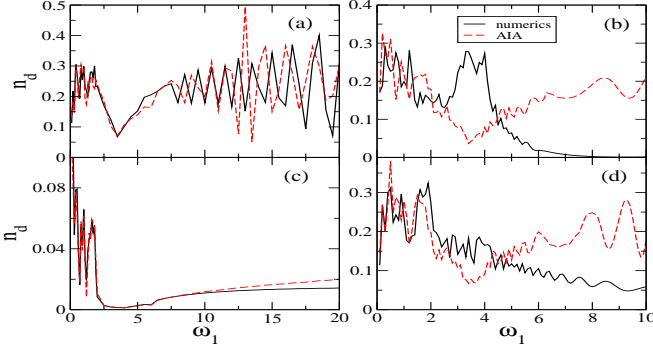


FIG. 4: (Color online) Comparison of exact numerical result (black solid line) for variation of n_d after $n = 100$ cycles as a function of ω_1 with that obtained from the adiabatic-impulse method (red dashed line) for (a) $r = 0$, (b) $r = 0.5$, (c) $r = 1$ and (d) $r = 2$. All parameters are same as in Fig. 1.

2. Analytic approaches

It is always good to have a theoretical handle of the results obtained using numerical integration of the Schrodinger equation in any dynamical problem. In what follows we will discuss the adiabatic-impulse approximation (AIA) and rotating wave approximation (RWA) for our drive with the two rate protocol to see how well they captures the dynamics at small and large frequency regimes respectively.

Adiabatic-Impulse approximation

The key aspect of the adiabatic-impulse approximation (AIA) is to divide the dynamics of a system subjected to a drive into two distinct regimes²³. The first is called the adiabatic regime where the rate at which the system Hamiltonian changes with time is small compared to the instantaneous energy gap; here the dynamics merely gathers a phase of the system wave-function. The second constitute the impulse regime where the rate of change of the Hamiltonian parameter is comparable to or larger than the instantaneous energy gap; in this regime, excitations are produced since the system can no longer follow the instantaneous ground state. In the context of the Hamiltonian given by Eq. 1, the latter region occurs when the system reaches a QCP. Therefore AIA becomes accurate for low-frequency drives where the small driving velocity forbids excitations to occur in the adiabatic regimes leaving the impulse regimes alone responsible for the defect productions.

The adiabatic-impulse formalism for a two rate protocol has been discussed at length in Ref.22 where periodic driving up to single cycle is studied. For the sake of continuity to the reader we here briefly outline the formalism before discussing the extension of it for many cycles of driving. To treat the dynamics of Eq. 1 subjected to a two-rate periodic protocol using the adiabatic-impulse approximation, we first identify the adiabatic and the impulse regions and the critical points $t_{1(2)\vec{k}}$ within a single cycle.

The gap, $2E_{+\vec{k}}$ (see Eq.6) reaches a minimum at $t = t_{1,2\vec{k}}$

at an avoided level crossing²² for which $\partial E_{+\vec{k}}/\partial t = 0$. Around $t = t_{1,2\vec{k}}$, the system enters the impulse regions and excitations are produced. One important aspect of AIA is to approximate the impulse region to be exactly at $t_{1,2\vec{k}}$. This is obtained by linearizing the Hamiltonian around $t_{1,2\vec{k}}$. A unitary transformation can be engineered to give the Hamiltonian at/ around impulse point a Landau-Zener (LZ) like form where linear time dependence appears in either diagonal or off-diagonal part of the Hamiltonian. The reader is referred to Ref.22 for the detailed calculations. The transformations finally give the Hamiltonian a LZ-like form whereby the transition probability at the impulse point $t_{a,\vec{k}}$ takes the form,

$$p_k^a = \exp[-2\pi\delta_k^a] \quad \text{with} \quad \delta_k^a = \frac{((\lambda_1(\omega_1 t_{a,\vec{k}}) - b_{\vec{k}})\dot{\lambda}_2(\omega_2 t_{a,\vec{k}}) - \lambda_2(\omega_2 t_{a,\vec{k}})\dot{\lambda}_1(\omega_1 t_{a,\vec{k}}))^2 \Delta_k^2}{((\dot{\lambda}_1(\omega_1 t_{a,\vec{k}}))^2 + \dot{\lambda}_2(\omega_2 t_{a,\vec{k}})^2 \Delta_k^2)^{3/2}} \quad (10)$$

With these and evaluating the the adiabatic evolution matrices between the critical points, we can reach the defect production probability $n_d(T)$ following Eq.8 with

$$|b_{+\vec{k}}|^2 = p_{\vec{k}}^1(1 - p_{\vec{k}}^2) + p_{\vec{k}}^2(1 - p_{\vec{k}}^1) - 2\sqrt{p_{\vec{k}}^1 p_{\vec{k}}^2(1 - p_{\vec{k}}^1)(1 - p_{\vec{k}}^2)}\cos(\theta_1 + \theta_2 + 2\xi_2) = P_{\vec{k}}(T). \quad (11)$$

Here $P_{\vec{k}}(T)$ is the excitation probability in the \vec{k} -th mode. The Stokes phase^{23,37,39} $\theta_a = \frac{\pi}{4} + \delta_k^a(\ln\delta_k^a - 1) + \arg[\Gamma(1 - i\delta_k^a)]$ and $\xi_1(\xi_2) = \int_{t_{1,\vec{k}}(t_{2,\vec{k}})}^{t_{2,\vec{k}}(t_{1,\vec{k}}+2\pi/\omega_1)} E_{+\vec{k}}(t)dt$. For n number of cycles, the transition probability is given by the expression²³

$$P_{\vec{k}}(nT) = P_{\vec{k}}(T) \frac{\sin^2 n\phi}{\sin^2 \phi} \quad \text{where} \quad \cos\phi = -\sqrt{(1 - p_{\vec{k}}^1)(1 - p_{\vec{k}}^2)}\cos(\theta_1 + \theta_2 + \xi_1 + \xi_2) - \sqrt{p_{\vec{k}}^1 p_{\vec{k}}^2}\cos(\xi_1 - \xi_2). \quad (12)$$

Within the adiabatic-impulse model, we can try to understand the freezing phenomena for driving up to, say, single cycle only. Following AIA, the transition between the adiabatic states can occur only at the QCP or avoided crossing points. With $\theta_1 = \theta_2 = \theta$ and $p_{\vec{k}}^1 = p_{\vec{k}}^2 = p_k$, say, for simplicity within Eq.11, we obtain $|b_{+\vec{k}}|^2 = 4p_k(1 - p_k)\cos^2\Theta$ where $\Theta = 2(\theta + \xi_2 - \pi/2)$. For freezing this quantity needs to be zero or very small for all \vec{k} values. Now $p_k = \exp(-2\pi\delta_k)$, as Eq.10 suggests. With very small or very large ω_1 values, δ_k becomes very large or small causing p_k to tend to 0 or 1 respectively. In either case, this makes $|b_{+\vec{k}}| \rightarrow 0$ causing freezing. Moreover, δ_k also depends on the second frequency ω_2 . So how fast $p_k \rightarrow 1$ for high frequencies also depends on ω_2 . That's why we see a pattern for lower cut-off of ω_1 in the XY chain results in Fig.2(b),(c) beyond which freezing continues at higher frequencies. So far we have not considered

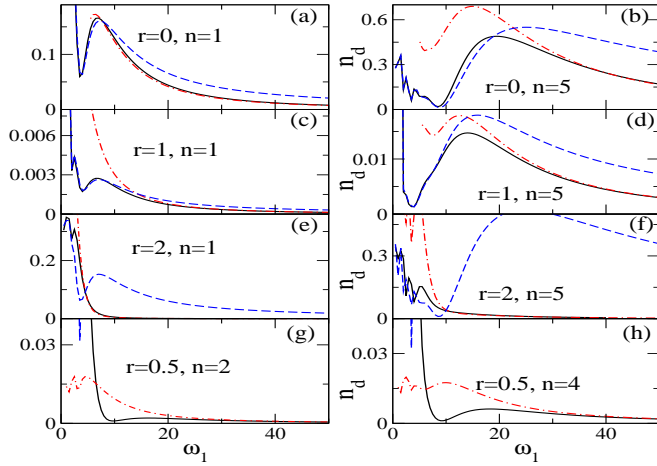


FIG. 5: (Color online) Comparison of exact numerical result (black solid line) for variation of n_d as a function of ω_1 with that obtained from the rotating wave approximation (red dash-dotted line) and adiabatic-impulse method (blue dashed line) for (a) $r = 0, n = 1$, (b) $r = 0, n = 5$, (c) $r = 1, n = 1$, (d) $r = 1, n = 5$, (e) $r = 2, n = 1$, (f) $r = 2, n = 5$, (g) $r = 0.5, n = 2$, (h) $r = 0.5, n = 4$. All parameters are same as in Fig.1.

the effect of angle Θ in this discussion. But in principle, $\cos\Theta$ can also be zero or very small enforcing the freezing criteria. This gives rise to the stueckelberg interference²³ and we may obtain pockets of dynamical freezing regime in the frequency space. 2D Kitaev model results display similar features in its defect density profile in Fig.3.

Comparison between exact numerical results and AI approximation can be seen in Fig.4. The defect density can nicely be reproduced using Adiabatic-Impulse approximation even after driving through many cycles. For small frequency the match is excellent while it deviates as higher and higher frequencies are considered. It gives an estimate of a higher cut-off of the small frequencies ω_1 up to which AIA holds good. Also we should point out here that the match is better for $r = 0$ and 1 as the Fig.4 demonstrates. This is because for $\omega_1 \neq \omega_2 \neq 0$, the time difference $n\frac{2\pi}{\omega_1}$ is not truly stroboscopic in nature and this fact need to be more suitably accommodated in this AIA formalism.

Rotating wave approximation

A rotating wave approximation (RWA) is a widely used approximation scheme in Quantum Optics and is often used to derive Rabi oscillations in a TLS. Within the formalism of rotating wave approximation (RWA), a transformation to the interaction picture or a rotating frame is made^{23,39} via an unitary transformation, which in our case is given by

$$|\psi_{\vec{k}}(t)\rangle = U_{\vec{k}}(t)|\psi'_{\vec{k}}(t)\rangle \quad \text{with} \\ U_{\vec{k}}(t) = \exp\left[-\frac{i}{2}(\eta - b_{\vec{k}}t)\tau_3\right] \quad \text{and} \quad \eta = \int \lambda_1 dt. \quad (13)$$

The objective, firstly, is to acquire a transformed 2×2 Hamil-

tonian $H_{\vec{k}}^L(t)$ that possess zero diagonal entries. In the remaining time-periodic off-diagonal part, a power series expansion is utilized²³ following the relation

$$e^{iz\sin\tau} = \sum_{n=-\infty}^{\infty} J_n(z)e^{in\tau}$$

where $J_n(z)$ denotes the Bessel's function of first kind with order n and argument z . The approximation comes when only the slowest moving component of the periodic expansion is kept in the Hamiltonian off-diagonal entries and thus it works well in high frequency limit. Thereafter a further rotation from basis $|\psi'_{\vec{k}}\rangle$ to $|\psi''_{\vec{k}}\rangle = \exp\left[-\frac{ib_{\vec{k}}t}{2}\tau_3\right]|\psi'_{\vec{k}}\rangle$ is performed that results in a time independent Hamiltonian

$$H_{\vec{k}}'' = \begin{pmatrix} -b_{\vec{k}}/2 & d(\vec{k})/2 \\ d(\vec{k})/2 & b_{\vec{k}}/2 \end{pmatrix}.$$

Here $d(\vec{k}) = \Delta_{\vec{k}}(J_m(A/\omega_1) + J_{-m}(A/\omega_1))/2$ for $r = m$, an integer. We should mention here that the final states for an integral r^{-1} can also be computed in a similar fashion at truly stroboscopic $n\tau$ times apart from the initial point, where n is an integer and τ is the lowest common multiple of $\frac{2\pi}{\omega_1}$ and $\frac{2\pi}{\omega_2}$ (See, for example, results in Fig. 5(g),(h)). This is because the diagonal and off-diagonal entries of $H_{\vec{k}}'$ can be swapped within a transformation $H \rightarrow e^{-\frac{i\pi\tau_3}{4}} H e^{\frac{i\pi\tau_3}{4}}$ and RWA can be performed over the transformed Hamiltonian.

At this stage, it is easy to solve the Schrodinger equation and obtain the transformed states. Back transformations from there can retrieve the original states and we can express the time evolution of states as

$$|\psi_{\vec{k}}(t)\rangle = \exp\left[-i\frac{d(\vec{k})t}{2}\tau_1\right]\exp\left[\frac{i}{2}(b_{\vec{k}}t - \eta)\tau_3\right]|\psi_{\vec{k}}(0)\rangle. \quad (14)$$

The formalism thus comes in steps, each of which involves a rotation of the wave-function basis. The approximation comes when the time dependent periodic function, which can be written as a sum over Bessel's functions times exponentials, is replaced with only the smallest (if not resonant) term present there. Naturally this is an approximation good at high frequencies as the other components become increasingly fluctuating with higher frequencies. We should mention here that RWA works much better if we look at time averaged variables after long times (*e.g.*, dynamical order parameter Q as calculated in Ref.21) as the highly fluctuating components can average out to zero. However for an observable, measured instantly at a time far from the initial time, the mutual cancellation of the number of highly fluctuating components give a good estimate as well.

Our RWA results, in comparison with exact numerics and AIA, are shown in Fig.5. The defect densities obtained using RWA can be seen to match with the exact results at high frequencies. We also notice that the comparison with RWA becomes better for longer times of driving if larger values of ω_1 are considered. To explain that we need to see that RWA is exact for $\omega_1 \rightarrow \infty$ and is a better approximation for larger

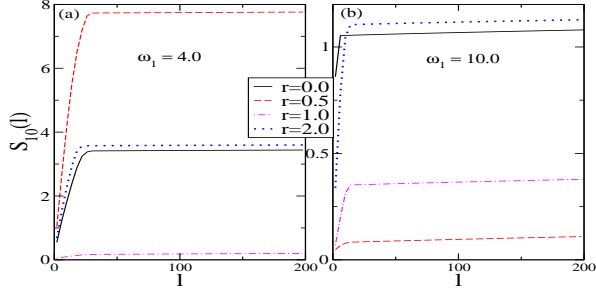


FIG. 6: (Color online) Entanglement entropy $S_n(l)$ after $n = 10$ cycles as a function of sub-system size l for different values of r at (a) $\omega_1 = 4.0$ and (b) $\omega_1 = 10.0$. Parameters used are same as in Fig.1.

ω_1 . But at the same time, approximation is used in obtaining the expression $d(\vec{k})$ in the transformed Hamiltonian H_k'' . So the error in an instantaneous state measurement increases with longer t because of the factor $d(\vec{k})t$ appearing in the expression of the evolved wave-function (Eq. 14).

B. Entanglement generation

The Schrodinger time evolution of the ground state in a closed quantum many body system does not carry any entropy with it. Nevertheless, the states can get entangled and we can attach an entanglement entropy to the state as an estimate for such entanglement. The entanglement entropy $S_n(l)$ of a subsystem of size l within our free fermionic driven system can be obtained from the two-point fermionic correlators C_{ij} and F_{ij} :

$$C_{ij} = \frac{2}{L^d} \sum_{\vec{k} \in BZ/2} |a_{1,\vec{k}}(t)|^2 \cos[\vec{k} \cdot (\vec{i} - \vec{j})]$$

$$F_{ij} = \frac{2}{L^d} \sum_{\vec{k} \in BZ/2} a_{1,\vec{k}}^*(t) a_{2,\vec{k}}(t) \sin[\vec{k} \cdot (\vec{i} - \vec{j})]. \quad (15)$$

A block diagonal $2l^d \times 2l^d$ correlation matrix \mathcal{C} is constructed with $l \times l$ diagonal blocks $1 - C$ and C and off-diagonal blocks F and F^* respectively and then diagonalized to obtain the eigenvalues p_i 's^{29,30}. From there the entropy is obtained as $S_n(l) = -\sum_1^{2l} p_i \log(p_i)$.

Let us first look into any possible connection between entanglement and freezing. A perfect freezing keeps the state intact and hence the amount of entanglement remains the same. The initial state is the the many-body ground state, which for short-ranged Hamiltonian, within the gapped phases, generally remains unentangled. Thus the region of maximum freezing should appear with minimum values for $S_n(l)$ after the dynamics. That is exactly what is seen in Fig.6(a)-(b), for the freezing points depicted as in Fig.1(d). The near-zero entanglement estimates appear at points in (ω_1, r) plane, as mentioned early in section II-A-1.

Next we turn to a more general discussion on $S_n(l)$ in our

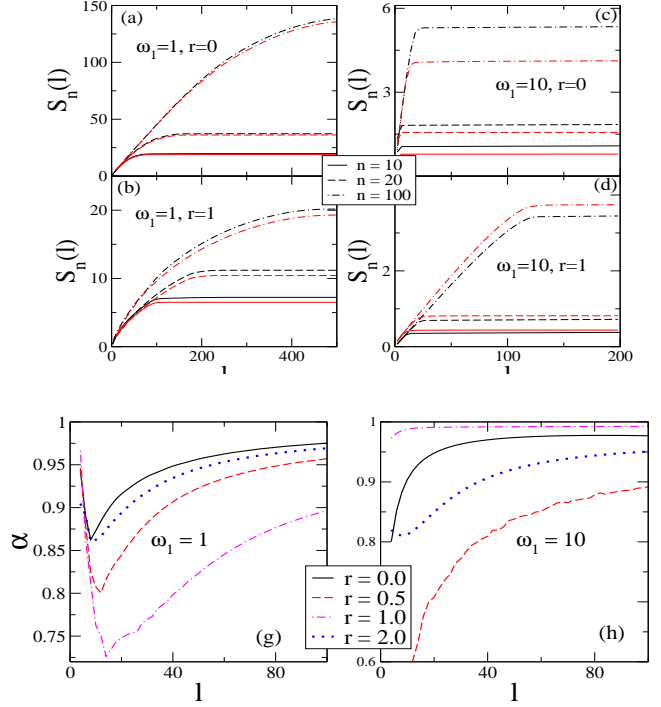


FIG. 7: (Color online) $S_n(l)$ versus l plots for $n=10$ (solid line), 20(dashed) and 100(dash-dotted) at (a) $\omega_1 = 1.0$, $r = 0$, (b) $\omega_1 = 1.0$, $r = 1$, (c) $\omega_1 = 10.0$, $r = 0$, (d) $\omega_1 = 10.0$, $r = 1$. Plots obtained within AIA are shown (red/gray lines) demonstrating better matches at smaller frequency $\omega_1 = 1$. Exponent α versus l for various r values with $n = 1000$ at (e) $\omega_1 = 1$ and (f) $\omega_1 = 10$ ($n = 10000$ is used for $r = 0$ here). All parameters are same as in Fig.1.

system. According to Hastings' theorem²⁸, a system with short range interactions, like a TFIM or TFXYM, should follow an area scaling for its entanglement entropy, *i.e.*, $S \sim l^{d-1}$ at dimensionality $d = 1$. For a periodic drive, we indeed find such behavior at $l \sim L/2$, starting from a cut-off l_c that increases with n , the number of drive cycles. For very large n , we get $l_c \sim O(L/2)$ and thus most of the time the entropy follows a non-area law of scaling. In fact it follows a volume law: $S \sim l^d$, for $n \rightarrow \infty$.

The results for $S_n(l)$ for a 1D TFXYM are shown in Fig.7. The entanglement entropies of subsystems A and B of a composite system in a pure state are equal. No entanglement can be there for a subsystem of null size. Hence we find $S(l = 0) = S(l = L) = 0$. The area law sprouts from the fact that bipartite entanglement in the ground state of a local Hamiltonian of a gapped system is proportional only to the boundary area between the two subsystems and hence it obeys: $S \sim l^{d-1}$. Now for very small l , the whole volume of the small subsystem contributes to entanglement, irrespective of whether the Hamiltonian is short-ranged or not. So we expect a volume law scaling for S at $l \ll L$. But as l increases, so does the volume-to-area ratio for the subsystem and the entanglement tends to follow the area scaling more and more. As the subsystem size exceeds the correlation length l_0 (which is

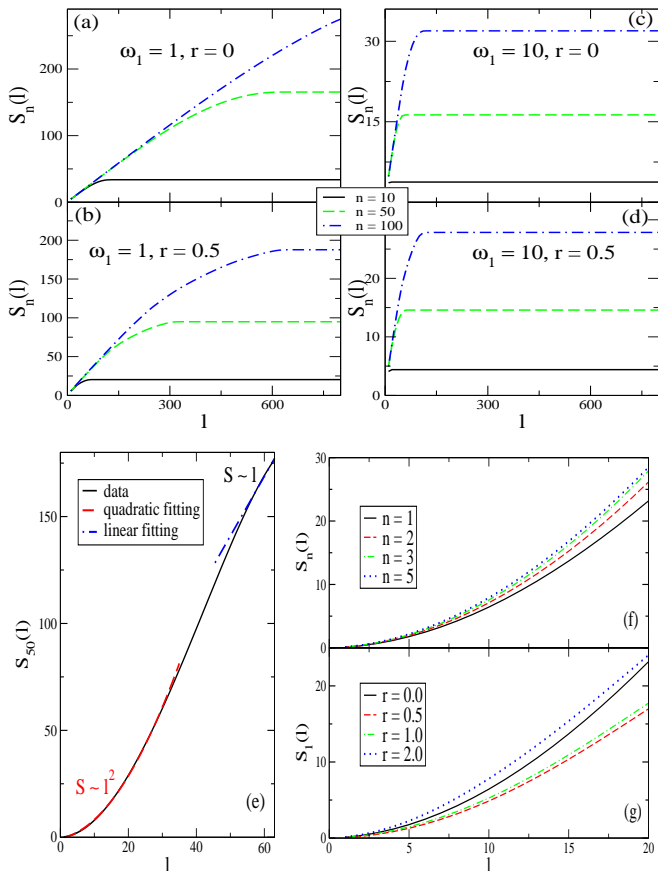


FIG. 8: (Color online) $S_n(l)$ versus l plots for $n=10$ (solid line), 50(dashed) and 100(dash-dotted) at (a) $\omega_1 = 1.0$, $r = 0$, (b) $\omega_1 = 1.0$, $r = 0.5$, (c) $\omega_1 = 10.0$, $r = 0$, (d) $\omega_1 = 10.0$, $r = 0.5$ for a Kitaev chain with parameters mentioned in section II-B. (e) Scaling of $S_{50}(l)$ with l for a 2D Kitaev model honeycomb lattice. Variation of (f) $S_n(l)$ for different n values at $r = 0$ and (g) $S_1(l)$ for different r values. A 100×100 rhomboidal mess is considered for the calculations in 2D Kitaev model. The parameter values are mentioned in section II-B.

of the order of the cut-off l_c) of the correlators C_{ij} and F_{ij} , area scaling appears to dominate in the $S_n(l)$ behavior (see Fig.7(a)-(d)). Thus we see a gradual cross-over from the volume scaling to area scaling behavior for $S(l)$ as l is increased from 0 up to $L/2$ with continuous regime of non-area-non-volume scaling behaviors in between. A large correlation in the time evolved state, however, pushes l_c more towards $L/2$.

In Fig.7(a)-(d), we further see that for a fixed (ω_1, ω_2) pair, the magnitude of $S(l)$ as well as the cut-off l_c to increase with n . The ground state of the gapped many-body system at $t = 0$ has very little entanglement and can thus be approximated as a product state. Starting from there, as the state is dynamically evolved for a long time, its spread within the Hilbert space keeps increasing and it becomes more entangled. A large l_c implies a larger subsystem size for which boundary rather than the whole volume becomes relevant for entanglement. For large n , correlation in the system increases and we need to

go to higher cut-off values where the smaller area-to-volume ratio can compensate for the larger correlations reaching out to area scaling more.

For very small as well as very large frequencies, a stroboscopic dynamics hardly see the state to evolve from its starting ground state and thus we obtain both freezing and unentangled final states. A fast driving reduces the correlation length which is manifested here from lower l_c values in Fig.7(c),(d) compared to that in Fig.7(a),(b) (as also in Fig.8(c),(d) compared to Fig.8(a),(b) from a 1D Kitaev model results). Also notice that the small frequency ($\omega_1 = 1$) entanglement entropy results of Fig.7(a),(b) can be well represented by Adiabatic-Impulse approximation (shown there as well), compared to similar results for large frequencies (such as $\omega_1 = 10$, as shown in Fig.7(c),(d)), as AIA supposedly works nicely for slow quenches.

If we define, for the entanglement entropy, an exponent of scaling²⁹ as $S \sim l^\alpha$, we see that α tends to unity, in our TFXYM chain, if l is gradually increased starting from zero or decreased starting from L . However this convergence towards unity is often non-monotonic. These results are demonstrated in Fig.7(e)-(f). For small n , entropy follows the area scaling above some cut-off values of l . But this cut-off increases with the values of n . In the plateau region above the cut-off, we witness the area scaling law to hold. But the region before cut-off becomes larger with n where we see the non-area, non-volume scaling laws to occur. For small ω_1 (Fig.7(a),(b)), the plateau region soon vanishes as n becomes large whereas a large ω_1 retains such behavior even for the large n values shown here in Fig.7(c)-(d). Fig.7(e)-(f) shows the evolution of scaling exponent α with l for a large $n = 1000$ cycle of driving and demonstrate the convergence of α towards unity. For a low frequency such as $\omega_1 = 1$, the scaling exponent goes to 1 rather nontrivially as can be seen at the smallest end of the sub-system size l (Fig.7(e)). For large ω_1 , the behavior is mostly monotonic. The convergence towards unity is rather slow for $r = 0$ (see Fig.7(f)). So a larger $n = 10000$ is used to see behavior of α in Fig.7(f). We see that for $r = 1$, α to converge to unity faster with l than other values of r shown in Fig.7 if larger frequencies (such as $\omega_1 = 10$) are considered. For small frequencies instead ($\omega_1 = 1$), such convergence is slowest for $r = 1$.

Thereafter we also study the entanglement entropy behaviors in Kitaev chain and 2D Kitaev model on a honeycomb lattice. We choose $J_1 = 0$, $J_2 = 1 + \cos(\omega_2 t)$, $J_3 = [1 + \cos(\omega_1 t)]/2$ for Kitaev chain and $J_1 = J_2 = [1 + \cos(\omega_2 t)]$, $J_3 = 4.5[2 + \cos(\omega_1 t)]$ for 2D Kitaev model so that both represent gapped systems at initial and stroboscopically advanced final times. The results from Kitaev chain, as shown in Fig.8(a)-(d), are in essence similar to 1D TFXYM results of Fig.7(a)-(d). In the 2D Kitaev model case, however, the entanglement entropy results bear the signature of dimensionality 2. Here we consider $l \times l$ rhombus shaped sub-systems within a system of size $L \times L$. For each such sub-system, the environment or the other partition within the system has a non-rhombus shape with area $L^2 - l^2$ and thus, unlike in 1D, we generally have $S_n(l) \neq S_n(L - l)$. Starting from zero, $S_n(l)$ grows with l , reaches a maximum at

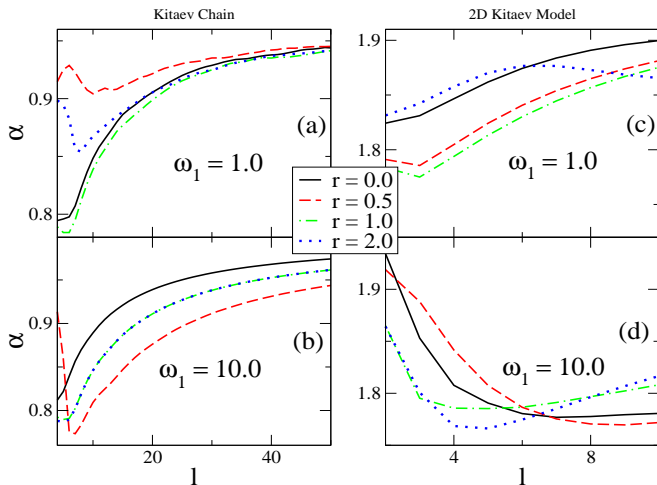


FIG. 9: (Color online) Exponent α versus l at various r values for (a),(b) Kitaev chain ($L = 2000$) with $n = 1000$ and (c),(d) 2D Kitaev model ($L = 200$) with $n = 100$. Results are shown for (a),(c) $\omega_1 = 1$ and (b),(d) $\omega_1 = 10$. Parameters used are those mentioned in section II-B.

an $l > L/2$ and then gradually decrease down to zero at $l = L$. For small l , volume scaling behavior is manifested and entropy scales as $S_n(l) \sim l^2$. As l value is increased the behavior gradually changes to a area law behavior with $S_n(l) \sim l$. Fig.8(e) illustrates such behaviors. We may point out here that had we considered a parallelogram shaped subsystem of size $l \times L$ (*i.e.*, cylindrical subsystem with periodic boundary conditions) instead, we would get, like in 1D cases, $S_n(l) = S_n(L - l)$ with $S_n(l)$ becoming symmetric about $L/2$. We find that in such situation entropy scales as $S_n(l) \sim l^{1/2}$ for small l values.

Similar to 1D model results, in 2D Kitaev model also $S_n(l)$ is found to increase with n (see Fig.8(f)) and by tuning r , we can tune the entropy as well. Fig.8(g) shows variation in $S_n(l)$ for $n = 1$ for different r values.

Finally if we look at the plots of exponent α versus l in Kitaev chain and 2D Kitaev model, we see that for very small l values the behavior, in general, is non-monotonic. We can also compare these plots with 1D TFXYM plots of Fig.7(e),(f). When we say that for small l , we see an volume scaling law to hold that gradually changes to a area scaling laws as l is increased in these short ranged integrable models, we expect the exponent α to start from d at very small l and to tend to $d - 1$ when l increases more and more. However, we find that the α vs. l plots for different r at very small l values (*i.e.*, for $l \ll L$) displays, rather, some non-monotonic behavior. This is certainly an interesting observation and deserves further investigation.

III. DISCUSSION

In this work, we have studied long-time periodic dynamics of a class of integrable models using a two-rate protocol.

Our results on a 1D TFXYM reveals that, starting the dynamics from ground state of the time dependent Hamiltonian, the periodic driving can lead to dynamical freezing when the second drive frequency $\omega_2 = r\omega_1$ is used as a tuning parameter. Such freezing starts developing from pretty small values of $\omega_1 \sim O(1)$ when $r \sim 1$ and it starts spreading along r , particularly if the system is driven for a few cycles, as frequency is increased further. New freezing zones starts sprouting out at intermediate frequencies $\omega_1 \sim O(10)$ for $r \sim 0.5$ or 2.0 and continues to grow similarly with higher ω_1 values. However, stroboscopic measurements after long driving sees the final state to get more and more steady with freezing scenario getting rarer compared to its transient profile. This is an expected trend and is independent of the models used, even though the distribution of the defect density in the frequency space varies, as confirmed from 2D Kitaev model results.

In order to have a analytical framework of the said dynamics, we extend the formalism of adiabatic impulse approximation for the two-rate protocol, as originally described in Ref.22, to the case of driving up to multiple cycles and for higher frequencies. It shows near-exact comparison with exact results at small frequencies (much higher than shown in Ref.22, and for far beyond merely a single cycle). We also develop a suitable extension of the rotating wave approximation scheme so that dynamics for fast quenching, in this case, can also be accounted for analytically. Our extension works for integral ω_2/ω_1 or ω_1/ω_2 values.

We also have a look at the entanglement entropy results in our dynamical system. We witness the unentangled nature of the ground states of our free fermionic Hamiltonians. The dynamic freezing regimes are found also to correspond to the regions of minimum entanglement in the system. Within the gapped phases, that we study, we find area scaling laws for entanglement entropy $S_n(l)$ to hold when driven not for long while genuine non-area scaling to occur under long driving. The scaling behavior tend to a volume scaling law for very large n . Within our two-rate protocol, a tuning with r resulting in huge alteration of the entropy content can always be commercially used in our favor. Our results both on TFXYM and Kitaev chain and 2D Kitaev model on honeycomb lattices demonstrate important behavior of the periodically driven (with a two-rated protocol) integrable models away from a QCP.

Our work can be well extended to studying the long-lived non-thermal steady states^{1,41} when driving periodically with a two rate protocol. The dynamical freezing, obtained in this work, can motivate further researches in the field of quantum computing, such as designing superconducting qubits⁴² or circuit QED devices⁴³. Moreover, finding the Floquet spectrum and the possible change in its topology, already observed for $r = 0$ case using a square wave protocol²⁹, can also give useful information on different dynamical phases and the transitions between them. Furthermore, we may also look into the entanglement spectrum and Schmidt gap in the dynamically evolved states and probe the possibilities of any topological transition⁴⁴ there. In short, the tuning knob r of the two rate periodic protocol opens up a world of opportunities enabling exploration of multifarious dynamical phenomena with huge

possibilities for numerous practical implementations.

Acknowledgement: The author benefited from discussions with K. Sengupta, H. K. Krishnamurthy, S. Mandal, A. Das,

A. Sen and S. N. Shevchenko. This work is financially supported by CSIR, India, under Scientists' Pool Scheme No. 13(8764-A)/2015-Pool.

-
- ¹ A. Polkovnikov, K. Sengupta, A. Silva, and M. Vengalattore, *Rev. Mod. Phys.*, **83**,863 (2011).
- ² J. Dziarmaga, *Adv. Phys.* **59**, 1063 (2010).
- ³ A. Dutta, U. Divakaran, D. Sen, B. K. Chakrabarti, T. F. Rosenbaum, and G. Aeppli, arXiv:1012.0653 (unpublished).
- ⁴ T. W. B. Kibble, *J. Phys. A* **9**, 1387 (1976); W. H. Zurek, *Nature (London)* **317**, 505 (1985).
- ⁵ A. Polkovnikov, *Phys. Rev. B* **72**, 161201(R) (2005).
- ⁶ K. Sengupta, D. Sen and S. Mondal, *Phys. Rev. Lett.* **100**, 077204 (2008).
- ⁷ D. Sen, K. Sengupta and S. Mondal, *Phys. Rev. Lett.* **101**, 016806 (2008).
- ⁸ A. Polkovnikov, *Phys. Rev. Lett.* **101**, 220402 (2008).
- ⁹ A. Chandran, A. Erez, S. S. Gubser, and S. L. Sondhi, *Phys. Rev. B* **86**, 064304 (2012).
- ¹⁰ S. Miyashita, K. Saito, and H. De Raedt *Phys. Rev. Lett.* **80** 1525 (1998).
- ¹¹ J. Gong, L. Morales-Molina, and P. Hanggi *Phys. Rev. Lett.* **103** 133002 (2009).
- ¹² F. Pollmann, S. Mukerjee, A. M. Turner, and J. E. Moore *Phys. Rev. Lett.* **102** 255701 (2009).
- ¹³ M. Heyl, A. Polkovnikov, and S. Kehrein *Phys. Rev. Lett.* **110**, 135704 (2013).
- ¹⁴ C. Karrasch and D. Schuricht, *Phys. Rev. B*, **87**, 195104 (2013); N. Kriel, C. Karrasch, and S. Kehrein *Phys. Rev. B* **90**, 125106 (2014).
- ¹⁵ F. Andraschko, J. Sirker, *Phys. Rev. B* **89**, 125120 (2014); E. Canovi, P. Werner, and M. Eckstein, *Phys. Rev. Lett.* **113**, 265702 (2014); M. Heyl, *Phys. Rev. Lett.* **115**, 140602 (2015).
- ¹⁶ S. Sharma, U. Divakaran, A. Polkovnikov, and A. Dutta, arXiv:1601.01637 (unpublished).
- ¹⁷ M. Lewenstein *Adv. Phys.* **56** 243 (2007).
- ¹⁸ E. C. G. Stueckelberg, *Helv. Phys. Acta* **5**, 369 (1932).
- ¹⁹ M. Demirplak and S. A. Rice, *J. Chem. Phys. A* **107**, 9937 (2003); *ibid.*, *J. Chem. Phys. B* **109**, 6838 (2005).
- ²⁰ W. D. Oliver, Y. Yu, J. C. Lee, K. K. Berggren, L. S. Levitov, and T. P. Orlando, *Science* **310**, 1653 (2005); M. S. Rudner, A. V. Shytov, L. S. Levitov, D. M. Berns, W. D. Oliver, S. O. Valenzuela, T. P. Orlando, *Phys. Rev. Lett.* **101**, 190502 (2008).
- ²¹ A. Das, *Phys. Rev. B*, **82**, 172402 (2010); S. Hegde, H. Katiyar, T. S. Mahesh, and A. Das, *Phys. Rev. B* **90**, 174407 (2014).
- ²² S. Kar, B. Mukherjee, and K. Sengupta, *Phys. Rev. B* **94**, 075130 (2016).
- ²³ S. N. Shevchenko, S. Ashhab, and F. Nori, *Phys. Rep.* **492**, 1 (2010).
- ²⁴ A. del Campo and K. Sengupta, *Eur. Phys. Jour. Sp. Topics*, **224**, 189 (2015)
- ²⁵ A. Dutta, A. Das, and K. Sengupta, *Phys. Rev. E* **92**, 012104 (2015).
- ²⁶ S. Mondal, D. Pekker and K. Sengupta *EuroPhys. Lett.* **100**, 60007 (2012).
- ²⁷ U. Divakaran, and K. Sengupta, *Phys. Rev. B* **90**, 184303 (2014).
- ²⁸ M. Hastings, *J. Stat. Mech.*, P08024 (2007).
- ²⁹ A. Sen, and K. Sengupta, arXiv:1511.03668 (unpublished).
- ³⁰ T. J. G. Apollaro, G. M. Palma, and J. Marino, *Phys. Rev. B* **94**, 134304 (2016).
- ³¹ J. D. Sau and K. Sengupta, *Phys. Rev. B* **90**, 104306 (2014).
- ³² S. Sachdev, *Quantum Phase Transitions* (Cambridge University Press, Cambridge, England, 1999).
- ³³ A. Kitaev, *Ann. Phys. (NY)* **321**, 2 (2006);
- ³⁴ D. Sen, K. Sengupta, and S. Mondal, *Phys. Rev. Lett.* **101**, 016806 (2008).
- ³⁵ X.-Y. Feng, G.-M. Zhang, and T. Xiang, *Phys. Rev. Lett.* **98**, 087204 (2007).
- ³⁶ A. H. Castro Neto, F. Guinea, N. M. R. Peres, K. S. Novoselov, and A. K. Geim, *Rev. Mod. Phys.* **81**, 109 (2009); S. Das Sarma, S. Adam, E. H. Hwang, and E. Rossi, *Rev. Mod. Phys.* **83**, 407 (2011); M. O. Goerbig, *Rev. Mod. Phys.* **83**, 1193 (2011); D. N. Basov, M.M. Fogler, A. Lanzara, F. Wang, and Y. Zhang, *Rev. Mod. Phys.* **86**, 959 (2014).
- ³⁷ B. Mukherjee, A. Sen, D. Sen, and K. Sengupta, *Phys. Rev. B* **94**, 155122 (2016).
- ³⁸ M. Z. Hasan and C. L. Kane, *Rev. Mod. Phys.* **82**, 3045 (2010); X-L Qi and S-C Zhang, *Rev. Mod. Phys.* **83**, 1057 (2011).
- ³⁹ S. Ashhab, J. R. Johansson, A. M. Zagoskin, and F. Nori, *Phys. Rev. A* **75**, 063414 (2007).
- ⁴⁰ S. de Sarkar, R. Sensarma, and K. Sengupta, *Phys. Rev. B* **92**, 174529 (2015).
- ⁴¹ I. Bloch, J. Dalibard, and W. Zwerger, *Rev. Mod. Phys.* **80**, 885 (2008); M. Eckstein, and M. Kollar, *Phys. Rev. Lett.* **100**, 120404 (2008).
- ⁴² J. Johansson *et al.*, *Phys. Rev. B* **80**, 12507 (2009).
- ⁴³ P. Neillinger *et al.*, arXiv:1603.00245 (unpublished).
- ⁴⁴ S. Mandal, M. Maiti, and V. K. Varma, *Phys. Rev. B* **94**, 045421 (2016).